Airborne Doppler Radar Observations of a Convective Storm

PETER S. RAY, DAVID P. JORGENSEN* AND SUE-LEE WANG†

National Severe Storms Laboratory/NOAA, Norman, OK 73069

(Manuscript received 10 December 1984, in final form 15 February 1985)

ABSTRACT

Airborne Doppler radar can collect data on target storms that are quite widely dispersed. However, the relatively long time required to sample an individual storm in detail, particularly with a single aircraft, and the amplification of the statistical uncertainty in the radial velocity estimates when Cartesian wind components are derived, suggests that errors in wind fields derived from airborne Doppler radar measurements would exceed those from a ground based radar network which was better located to observe the same storm. Error distributions for two analysis methods (termed Overdetermined and Direct methods) are given and discussed for various flight configurations. Both methods are applied to data collected on a sea breeze induced storm that occurred in western Florida on 28 July 1982. Application of the direct solution, which does not use the continuity equation, and the overdetermined dual-Doppler method, which requires the use of the continuity equation, resulted in similar fields. Since the magnitude of all errors are unknown and the response of each method to errors is different, it is difficult to assess overall which analysis performs better; indeed each might be expected to perform best in different parts of the analysis domain. A flexible collection strategy can be followed with different analysis methods to optimize the quality of resulting synthesized wind fields.

1. Introduction

The use of multiple ground-based Doppler radars to deduce the windflow within convection has become fairly routine since the mid 1970s. Most analyses have used the principle that with two or more Doppler radars viewing a common point in space, it is possible to deduce three components of the wind, usually also employing the equation of mass continuity. Major error sources are statistical uncertainty in the measurements, poor estimates of the divergence at the surface and at cloud top, inexact boundary conditions, uncertainty in particle fallspeed, advection errors, and storm evolution during the several minutes required to collect the data. These errors are amplified by an amount depending upon the geometric relationship of the radars and the storm. These errors are also important for airborne Doppler radar. The utility of an airborne Doppler radar is its portability and the wealth of other instruments that complete the complement of aircraft sampling systems.

There are many areas (such as over oceans) where it is not practical to use ground based radars. In addition, for storms which may not predictably occur near a desired location, the airborne radar offers portability to extend the area and time of study. Also, frequently the airborne system can sample at a higher spatial resolution than is often possible with a ground based radar.

Jorgensen *et al.* (1983) gave a description of the NOAA P-3 and its airborne Doppler radar and presented an analysis which was a simplification of the direct method as described in this paper. Hildebrand *et al.* (1983) further discussed and evaluated the applications of airborne Doppler radar. They found good agreement between airborne measured wind fields and those derived from ground based Doppler radars.

Figure 1 is a schematic of the NOAA P-3 equipped with a tail mounted X-band (3 cm) Doppler radar. This radar scans in a vertical plane that is approximately perpendicular to the flight track, analogous to an RHI scan from a ground based radar. As the aircraft translates through the air the radar beam prescribes a helical path through space. The typical antenna rotation rate is 60° s^{-1}. Combining this rotation rate with the aircraft's nominal ground speed (140 m s^{-1}) results in a horizontal resolution of approximately 0.85 km. The plane also is equipped with an incoherent C-band (5 cm) horizontally scanning radar mounted below the fuselage. Data from both of these radars can be digitally recorded. For pilot use, a forward looking 5 cm incoherent radar is located in the aircraft's nose. (See Jorgensen, 1984, for a description of the noncoherent radar systems.)

This study examines the characteristics of different approaches to synthesizing data from the airborne

* Atlantic Oceanographic & Meteorological Laboratory/HRD, NOAA, Miami, FL. Present affiliation: NOAA/ERL/Weather Research Program, Boulder, CO 80303.

† Supported by the Cooperative Institute for Mesoscale Meteorological Studies (CIMMS), University of Oklahoma, Norman, OK 73019.

© 1985 American Meteorological Society

Unauthenticated | Downloaded 09/23/21 10:07 AM UTC

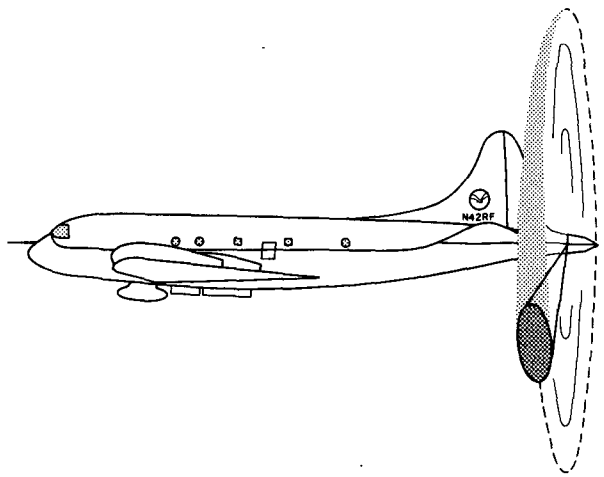

FIG. 1. Schematic of the NOAA P-3 aircraft showing the tail Doppler radar which rotates in RHI-type scans about the plane axis.

Doppler radar. The expected error fields are related to analogous situations from ground based radars for interpretation in the more familiar scanning reference frame of ground radars.

2. Analysis approach

Figure 2 schematically illustrates the sampling geometry of the airplane data collection. This schematic assumes that all flight induced motions, resulting from pitch, roll, and drift biases have been removed and that the plane is flying level, with the radar oriented at right angles to the flight path as projected onto the ground. The azimuth (using conventional notation) is given by θ, the clockwise direction from north. The elevation angle ϕ, which ranges from $\pm 90°$, is defined as $0°$ when the antenna is horizontal. The radar, located at a point defined by (x_i, y_i, z_i) observes a point P defined by (R_i, θ_i, ϕ_i) at (x, y, z) in space. Then the synthesis can be treated identically to that of ground based radars where

$$u(x - x_i) + v(y - y_i) + W(z - z_i) = V_i R_i \quad (1a)$$

$$R_i = [(x - x_i)^2 + (y - y_i)^2 + (z - z_i)^2]^{1/2} \quad (1b)$$

$$w = W - V_t \quad (1c)$$

where u, v and w are the wind components in the x, y and z directions, respectively, V_i the radial component of hydrometeors, and V_t is the mean terminal fallspeed of the scatterers within the pulse volume. Particle fall speed W can be obtained from (1c).

a. Direct method

As the airplane moves it can view the same point from a number of different orientations. If they are adequately separated in space (1a) can be solved for the wind components. To accommodate all the possible observations from the flight track, it is convenient to employ least-squares methodology, which is the maximum likelihood estimate if the errors are normally distributed. Mathematically, this technique can be expressed as:

$$\begin{bmatrix} \Sigma(x - x_i)^2 & \Sigma(x - x_i)(y - y_i) & \Sigma(x - x_i)(z - z_i) \\ \Sigma(x - x_i)(y - y_i) & \Sigma(y - y_i)^2 & \Sigma(y - y_i)(z - z_i) \\ \Sigma(x - x_i)(z - z_i) & \Sigma(y - y_i)(z - z_i) & \Sigma(z - z_i)^2 \end{bmatrix} \begin{bmatrix} u \\ v \\ W \end{bmatrix} = \begin{bmatrix} \Sigma V_i(x - x_i)R_i \\ \Sigma V_i(y - y_i)R_i \\ \Sigma V_i(z - z_i)R_i \end{bmatrix}, \quad (2)$$

where the coefficient matrix **[C]** is symmetric and whose inverse is denoted by **[B]** = **[C]**$^{-1}$. If σ_{vi}^2 is the error variance in the radial velocity estimate from the i^{th} observation point, then the variances of the estimator of the synthesized wind components are given by

$$\begin{bmatrix} \sigma_u^2 \\ \sigma_v^2 \\ \sigma_W^2 \end{bmatrix} = \begin{bmatrix} \Sigma\sigma_{vi}^2(B_{11}(x - x_i)R_i + B_{12}(y - y_i)R_i + B_{13}(z - z_i)R_i)^2 \\ \Sigma\sigma_{vi}^2(B_{12}(x - x_i)R_i + B_{22}(y - y_i)R_i + B_{23}(z - z_i)R_i)^2 \\ \Sigma\sigma_{vi}^2(B_{13}(x - x_i)R_i + B_{23}(y - y_i)R_i + B_{33}(z - z_i)R_i)^2 \end{bmatrix}. \quad (3)$$

In practice, to determine $(\sigma_u^2, \sigma_v^2, \sigma_W^2)$ requires at least three estimates from at least three distinctly different aircraft positions. This requirement implies a "U"-shaped, triangular or box-shaped flight pattern. Even so, the error in σ_W^2 will be unbounded at flight level since no component of the vertical wind is observed when the antenna points horizontally. This method of wind field retrieval works best when relatively large elevation angles are used, i.e., the aircraft is relatively close to the target. However, since the radar measures particle motion, uncertainty in particle fall speed can be large for certain regions in deep convection. These uncertainties relate directly to the error in the synthesized vertical wind.

To overcome the limitations presented in the solution to (3), variations on the direct method can be employed. For example, the horizontal wind components can be computed with (2). The horizontal

Unauthenticated | Downloaded 09/23/21 10:07 AM UTC

wind field is not contaminated by uncertainties in V_t. Then the vertical component may be obtained from the equation of continuity

$$\frac{\partial u}{\partial x} + \frac{\partial v}{\partial y} + \frac{\partial w}{\partial z} - \kappa w = 0, \tag{4}$$

where κ is the logarithmic rate of change of density with height.

b. Overdetermined dual-Doppler method

A second method, described in Ray and Sangren (1983), considers the observations in the framework of an overdetermined dual-Doppler radar synthesis (ODD) technique which incorporates (4) to close the equation set. Using standard least squares methodology the u and v components can be written:

$$u = \frac{\Sigma R_i V_i (x - x_i)\Sigma(y - y_i)^2 - \Sigma R_i V_i (y - y_i)\Sigma(x - x_i)(y - y_i)}{\Sigma(x - x_i)^2\Sigma(y - y_i)^2 - [\Sigma(x - x_i)(y - y_i)]^2} + W\frac{[\Sigma(y - y_i)(z - z_i)\Sigma(x - x_i)(y - y_i) - \Sigma(y - y_i)^2\Sigma(x - x_i)(z - z_i)]}{\Sigma(x - x_i)^2\Sigma(y - y_i)^2 - [\Sigma(x - x_i)(y - y_i)]^2} \tag{5a}$$

$$v = \frac{\Sigma R_i V_i (y - y_i)\Sigma(x - x_i)^2 - \Sigma R_i V_i (x - x_i)\Sigma(x - x_i)(y - y_i)}{\Sigma(x - x_i)^2\Sigma(y - y_i)^2 - [\Sigma(x - x_i)(y - y_i)]^2} + W\frac{[\Sigma(x - x_i)(y - y_i)\Sigma(x - x_i)(z - z_i) - \Sigma(x - x_i)^2\Sigma(y - y_i)(z - z_i)}{\Sigma(x - x_i)^2\Sigma(y - y_i)^2 - [\Sigma(x - x_i)(y - y_i)]^2}. \tag{5b}$$

The vertical component of air motion w and refined estmates of u and v are determined then from (4), (5a) and (5b) through iteration.

The variance of the estimator of the deduced wind component can then be expressed as

$$\sigma_u^2 = \Big\langle \sum_i \sigma_{vi}^2 \{R_i(x - x_i)[\Sigma(y - y_i)^2] - R_i(y - y_i)[\Sigma(x - x_i)(y - y_i)]^2 + \sigma_W^2[\Sigma(y - y_i)^2\Sigma(x - x_i)(z - z_i) - \Sigma(x - x_i)(y - y_i)\Sigma(y - y_i)(z - z_i)]^2\Big\rangle \times \{\Sigma(x - x_i)^2\Sigma(y - y_i)^2 - [\Sigma(x - x_i)(y - y_i)]^2\}^{-2} + \mathrm{cov}(u, w), \tag{6a}$$

$$\sigma_v^2 = \langle \Sigma\sigma_{vi}^2\{R_i(y - y_i)(\Sigma(x - x_i)^2 - R_i(x - x_i)[\Sigma(x - x_i)(y - y_i)]\}^2 + \sigma_W^2[\Sigma(x - x_i)^2\Sigma(y - y_i)(z - z_i) - \Sigma(x - x_i)(y - y_i)\Sigma(x - x_i)(z - z_i)]^2\rangle \times \{\Sigma(x - x_i)^2\Sigma(y - y_i)^2 - [\Sigma(x - x_i)(y - y_i)]^2\}^{-2} + \mathrm{cov}(v, w), \tag{6b}$$

where

$$\sigma_W^2 = \sigma_w^2 + \sigma_{v_t}^2,$$

$$\sigma_w^2 = \frac{1}{2}\left[1 + \left\{\frac{(1/\Delta z) - (\kappa/2)}{(1/\Delta z) + (\kappa/2)}\right\}^2\right]\sigma_{w_{k+1/2}}^2 + \frac{\sigma_u^2}{2\Delta x(1/\Delta z + (\kappa/2)]^2} + \frac{\sigma_v^2}{[2\Delta y(1/\Delta z) + (\kappa/2)]^2} \tag{6c}$$

for downward integration where k is an index denoting height level, derivatives have been approximated by centered differences, and the integration approximated through the trapezoidal rule. The $\sigma_{v_t}^2$ is the variance of the fall speed estimate. In storm regions containing large hail, incorrect assignment of the proper hail terminal velocity can dominate the $\sigma_{v_t}^2$ error term.

A simplification of the ODD technique was first described by Jorgensen *et al.* (1983) for the special case of two quasi-orthogonal flight legs. In their analysis the data in the vicinity of each grid point are tabulated for each flight leg. If more than one radial gate falls in a particular grid volume, the estimates are averaged to yield the single estimate per flight leg. A second field of estimates is then produced from the second flight leg. The two fields are then combined resulting in a horizontal wind field. This compositing reduces the number of observations processed in the next step (either a dual-Doppler or direct approach) to one observation per leg at each grid point. However, the ODD analysis used here treats each observation separately. For two nearly straight intersecting flight legs, one would expect both approaches to yield similar results. As flight patterns become more irregular, larger errors or greater complexity in specifying legs would be expected if the data are not treated separately. The analysis of Jorgensen *et al.* (1983) neglected vertical motions because

Unauthenticated | Downloaded 09/23/21 10:07 AM UTC

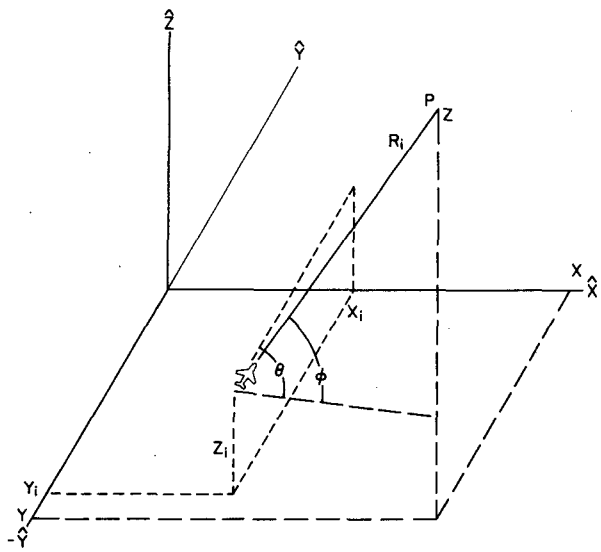

FIG. 2. Schematic of a plane located at (x_i, y_i, z_i) with an antenna observing a volume at point P. This location at (x, y, z) is defined by the antenna by θ_i (clockwise from north) and ϕ_i (elevation) and range R_i.

of the stratiform nature of the weather system. They also restricted the elevation angles used in their analysis to ±20° from the horizontal which yields a maximum (at 20°) of 34% of the vertical motion not included in the solution of (5). Since w typically decreases in nonconvective precipitation as the elevation angles become extreme, the effect of neglecting the second term in (5) was considered to be small.

c. *Geometric considerations*

To anticipate the quality of data from a typical "L"-shaped flight pattern the expected uncertainty of the vertical wind component was computed using Eq. (6c) for a 14 km tall storm. To assist comparison with ground-based radars this simulated flight is along $z = 0$ or at the earth's surface. The errors at 6 km altitude are shown in Fig. 3. The assumed σ_{vi}^2 is 1 m^2 s^{-2}. Between the 100 m^2 s^{-2} isopleth and the flight legs, the errors increase rapidly to very large values, becoming unbounded along the flight leg. To interpret these results we look at the dual-Doppler radar analog for five representative points within the volume viewed by the aircraft. In each of the five small panels, a ground based radar is located at the open end of each heavy line. The intersection of the heavy lines is the point which corresponds to the indicated spot in the airborne Doppler radar case. In general, every point in the airborne Doppler radar space corresponds to a particular and different placement of two ground based radars. There is typically an error minimum perpendicular to the line bisecting the radar baseline at a distance roughly equivalent to the radar separation. Figure 3 implies that to adequately sample the horizontal wind at the storm top and bottom, the airplane must be 2–3 times further from the storm than the difference in the height of the aircraft and the storm top or base. This condition is most nearly met on the extreme ends of long flight legs. However, note that at these points the observations are separated by the maximum in time and the beam volumes are the largest. Smaller values of σ_w^2 at large distances from the flight legs result from improved estimates of the horizontal winds involving smaller extremes in elevation angles and the relationship of σ_w^2, through (6c), to errors in the horizontal motion field. Increased uncertainty in $\sigma_{v_t}^2$ would, of course increase errors, particularly close to the flight track where radar elevation angles are larger.

It is clear that the reason the errors are so large close to the flight legs is due to the large error in determining the horizontal wind at upper levels when the elevation angles are large. This is equivalent to two ground based radars resolving the winds close to one or more of the radars. In this condition, the observation point is also close to the radar base line. The uncertainty in the component normal to the base line feeds into the uncertainty of the vertical motion through the continuity equation. Through (6a) and (6b) the vertical velocity uncertainty also continues to increase errors in the horizontal winds, even at lower elevations, until exactly at flight altitude where there is no coupling. The horizontal wind at and near flight altitude is very well determined by this flight path. Another concern centers around whether the CFL (Courant, Friedrich, Levy) criterion (Haltiner and Williams, 1980)

$$\max\left[\frac{\tan\phi\Delta z}{\Delta x,\ \Delta y}\right] \leqslant 1,$$

is sufficiently satisfied to insure convergence of the iteration procedure. Over most of the volume, one would expect convergence since $\Delta_x = \Delta_y = \Delta_z$ and typical elevation angles are $\leqslant 45°$.

Given these results it is useful to examine the expected error from other flight geometries. Figure 4 shows three different flight patterns in which the legs form acute, right and obtuse angles at their apex. The stippled area represents the common area viewed by the radar from both flight legs. Representative analysis points within the sample space are labeled A through D. For each of these flight tracks the sample point is chosen so that the equivalent dual-Doppler spacing in the analogue is the same. The dual-Doppler analogue for all these cases is found in the lower right panel of Fig. 4. Examination reveals that the flight pattern which contains the point labeled D contains the area with the least error, but the smallest common sampling area. Whereas if the plane flew a path that straddled the storm with legs which formed an acute angle as represented by point C, the error

Unauthenticated | Downloaded 09/23/21 10:07 AM UTC

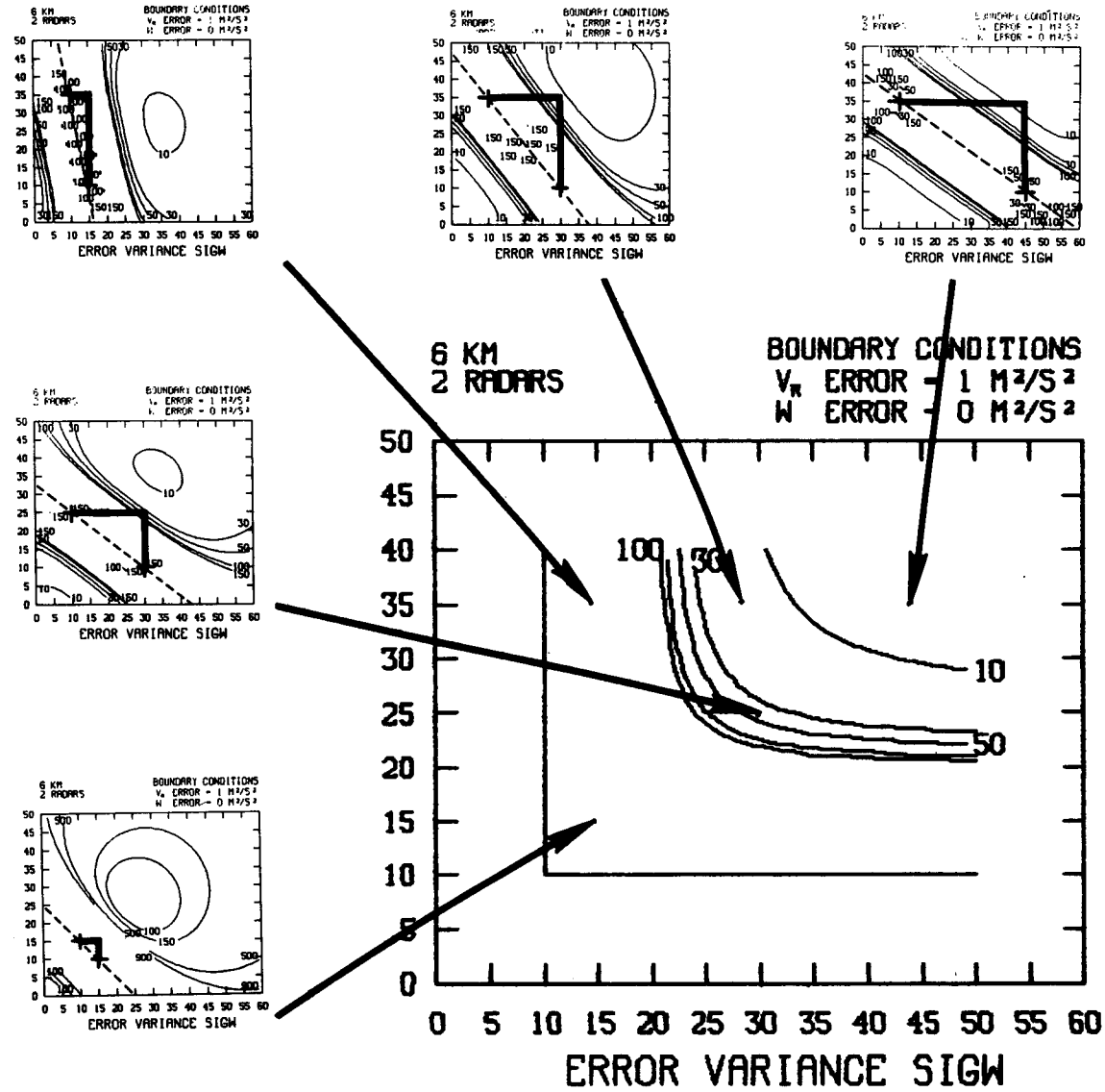

FIG. 3. Expected errors in the vertical velocity component at 6 km altitude from an airborne Doppler radar flying an "L"-shaped pattern near the earth's surface. The errors are contoured in units of $m^2 s^{-2}$. At five selected points, analogous ground-based dual-Doppler error fields have been computed with the radar locations indicated by crosses. The intersection of the radials (thick solid lines, always at right angles) is the point which is most nearly the same as the referenced point in the aircraft error field. Axes are distance in km. The dual-Doppler base line is indicated by the dashed line.

would be large. The error is generally smaller in the area outside the area between the flight legs as illustrated by the point B. This pattern also gives a large area of common coverage. As the angle (β) formed by the flight legs of length l becomes smaller, the region defined by interior points such as C and D becomes smaller while the area outside the region embraced by the legs becomes larger. However, as β decreases the radar separation likewise decreases and the angle between the beams approaches 0° in the dual-Doppler analog. The errors rapidly increase when the angle between the beams is <20°.

Another important case involves the combined use of a ground-based radar with the airborne Doppler radar. An example of the distribution of the expected errors is given in Fig. 5. The figure format is the same as Fig. 3 with six locations isolated for comparison with the dual Doppler ground-based radar analog. Note that the angle formed by the beam intersection varies with aircraft position. The minimum error occurs for beam intersections that are near 45°. An intersection angle near 90° implies a position close to the plane's position and for this case the errors are expected to be large there due to poor estimates of

Unauthenticated | Downloaded 09/23/21 10:07 AM UTC

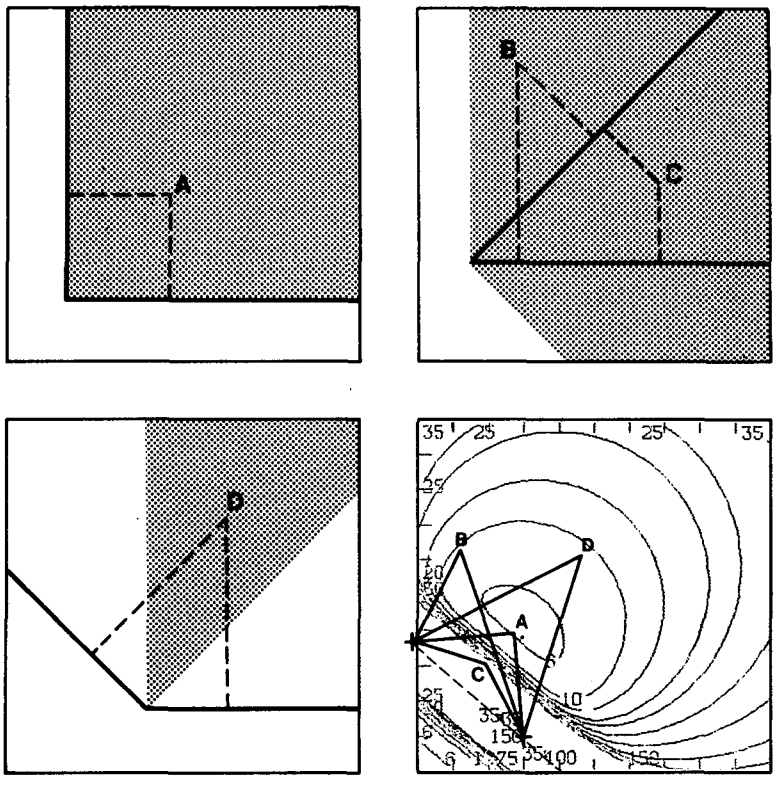

FIG. 4. Comparison of three alternative flight tracks (a–c) and relative errors for the flights for sample aircraft position which are equally spaced. The stippled portion represents the common area viewed by a side looking Doppler radar aboard an airplane from both legs of its flight. The contoured figure (d) shows the error in the vertical velocity component (in $m^2\ s^{-2}$) at 6 km from radars, integrating down from the 14 km storm top. It is assumed that the errors of each radial wind component interpolated to a grid point is 1 $m^2\ s^{-2}$. The angles labeled A–D serves to relate points in the aircraft data field with the corresponding points in the ground-based dual-Doppler error field.

the horizontal wind at the storm top and bottom. Like Fig. 3, the error is a minimum at relatively long ranges from both participating radars. However, unlike the pattern illustrated in Fig. 3, the plane does not need to fly long distances to get to the needed sampling points.

Figures 3 and 5 can be further explained by examining the simple case of two intersecting flight tracks using the Boussinesq approximation and the direct method. The error of the vertical velocity at level N is:

$$\sigma_w^2 = \sum_1^N \sigma_H^2. \tag{7}$$

The error in the vertical velocity is equal to the sum of the horizontal (divergence) errors through N levels and

$$\sigma_H^2 = \frac{1}{\sin^2\beta}\left[\frac{\sigma_1^2}{\cos^2\phi_1} + \frac{\sigma_2^2}{\cos^2\phi_2}\right], \tag{8}$$

where σ_1^2 and σ_2^2 are the assumed error variances from each observation.

As illustrated in Fig. 6, the contribution from the first term in Eq. (8) increases rapidly for β less than 45°. Also, since $1/\cos^2\phi = 1/(1 - \sin^2\phi)$ the contribution of errors obtained from elevation angles greater than 45° will dominate the sum in Eq. (7). At each level, for a flight of two straight legs, only range determines the error distribution since β is constant over the entire field. Thus, we can see in Fig. 3 how (due to the assumptions of the aircraft flight level close to the ground and storm top of 14 km) the aircraft must be at a range > 14 km away from the storm to deduce reasonable windfields at the storm top. This can be extended easily to Figs. 4 and 5.

3. Case example

On the afternoon of 28 July 1982, the NOAA P-3 collected Doppler radar data on a convective storm embedded in the sea-breeze convergence zone along

Unauthenticated | Downloaded 09/23/21 10:07 AM UTC

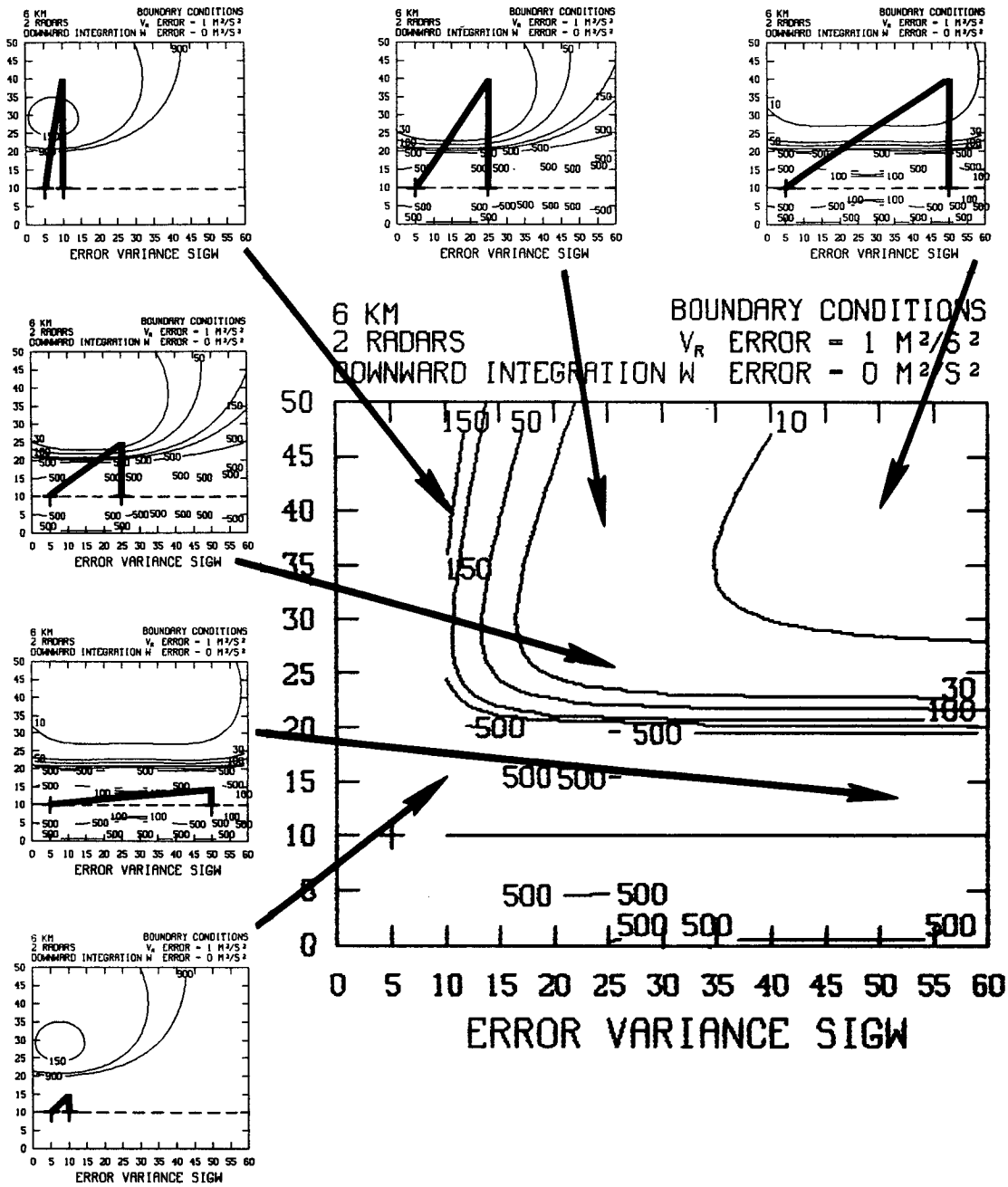

FIG. 5. Expected errors in the vertical velocity component at 6 km altitude from a ground based radar and side-looking Doppler radar aboard an airplane flying directly toward or away from the ground-based radar. The flight path is indicated by the horizontal line at $y = 10$. The errors are expressed in $m^2 s^{-2}$. At six selected points the analogous dual Doppler error fields have been computed with the intersections of the radial from the ground radars representing the analogous point to the indicated point on the larger aircraft/ground-based radar contour diagram. Axes are distance in km. Other details are the same as Fig. 3 caption.

the southwestern Florida coast as part of the NOAA/Hurricane Research Division's program to study the evolution of the sea breeze circulation. The portion of flight analyzed here was south along the west coast of Florida then east for about 40 km and then north again. The flight path is shown relative to local landmarks in Fig. 7. The data used here were collected during the flight for the period from 1636:49 to 1651:37 (EST). Figure 7 also shows the echo area determined by the aircrafts horizontally scanning C-band

Unauthenticated | Downloaded 09/23/21 10:07 AM UTC

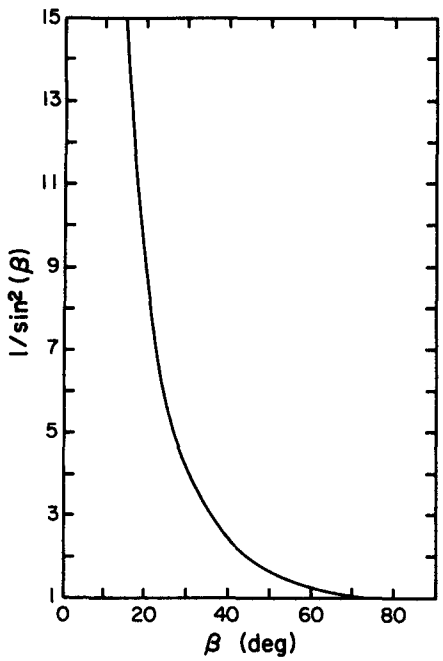

FIG. 6. Plot of $1/\sin^2\beta$ as a function of β.

radar. Intensities between 25–30 dBZ and 35–40 dBZ are stippled. The echo pattern reveals a quasi-linear, north–south precipitation line containing embedded cells with higher reflectivity. The portion of the complex selected for analysis is indicated by the square enclosed by the flight legs. The analysis domain is 30 km on each side with grid points spaced 1 km horizontally and 1.2 km vertically. During data collection the airplane was flying at an altitude about 0.3 km above the ground. The convection line appeared to be nearly steady during the data collection period but moved westward at about 2 m s^{-1}.

Using the sea breeze flight pattern, expected errors due to the propagation of uncertainty in radial velocity estimates are examined for both the ODD and direct analysis methods. In all the error figures the interpolated radial velocity error is assumed to be 1 m^2 s^{-2}. In practice, the actual grid point error may be less due to averaging several observations in the interpolation process; error fields may be correspondingly scaled. Figure 8a shows the expected uncertainty in vertical velocity estimates for the overdetermined dual-Doppler method at 4 km. Errors are minimized near the top center of the analyses domain. The 30 × 30 km square analysis domain is indicated by the box. At the bottom of the analysis domain the errors become very large since these points are "close" to the three flight tracks, which has been shown to be equivalent to a ground-based radar baseline. This error pattern and the value of the error at any point varies only slowly with height. The error pattern of

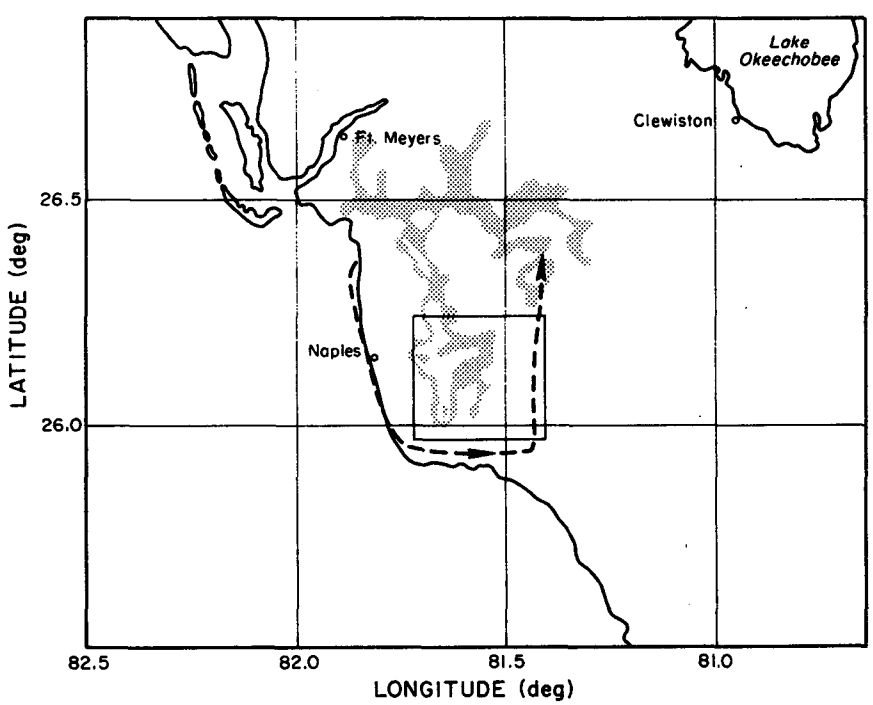

FIG. 7. Composite radar echo illustrating the area of data collection, flight path (thick dashed line), radar echo pattern (near ground) and analysis domain (box). The airplane was flying at about 0.3 km. Stippled echoes are 25–30 and 35–40 dBZ. The clear area between stippling represents reflectivities between 30–35 dBZ. The radar pattern was derived from a composite of 30 sweeps from the C-band lower fuselage radar.

Unauthenticated | Downloaded 09/23/21 10:07 AM UTC

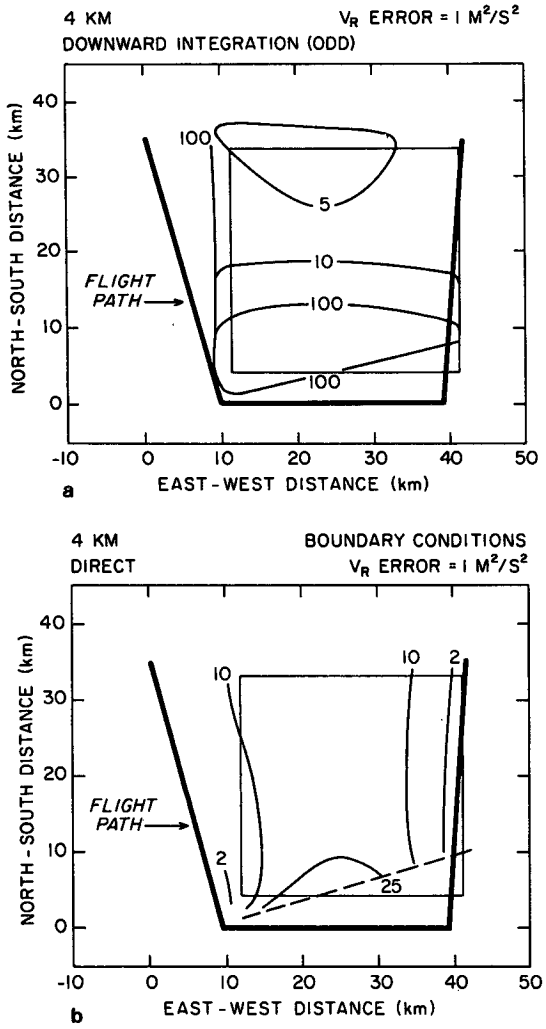

FIG. 8. Expected vertical velocity error variances ($m^2 s^{-2}$) 4 km altitude for (a) overdetermined dual Doppler (ODD) and (b) direct solution methods. Errors are normalized to assume interpolated u and v errors of 1 $m^2 s^{-2}$ in both cases. Dashed line in (b) represents a data boundary. Axes are distance in km.

horizontal divergence is likewise similar to the field shown here.

The expected error in vertical velocity at 4 km altitude for the direct solution method is shown in Fig. 8b. For this analysis method, the error in W is proportional to $1/z^2$ where z is the height of the data point above or below the plane's altitude. Thus, we expect the error to decrease with increasing height. For a perfect U shaped pattern, with two parallel legs, there is no variation in the error for a given height parallel to the parallel leg. The error is a minimum over either parallel leg.

The horizontal flow field within the analysis domain is shown for both the ODD and direct analyses methods in Fig. 9. The storm was moving slowly (2 m s^{-1}) to the west and these winds are storm relative. The data were advected to their probable position at 1644 EST before further processing. To preserve the proper perspective, the radar position must similarly

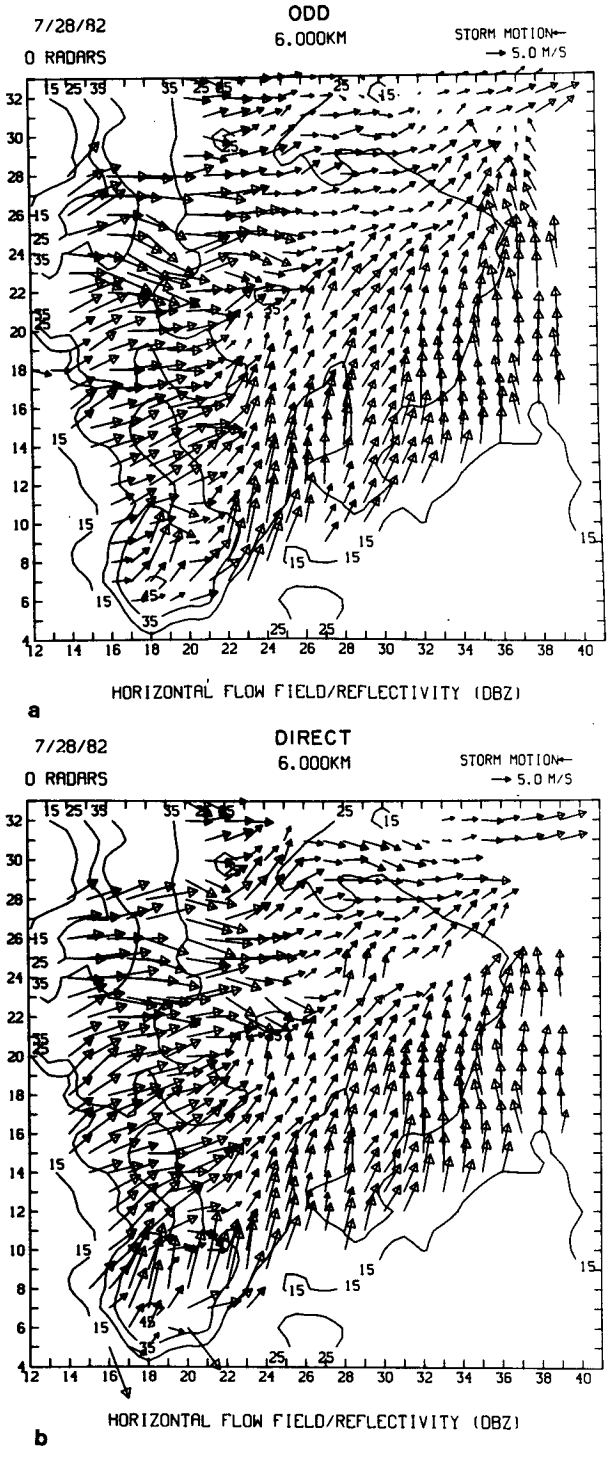

FIG. 9. Horizontal–vertical wind fields from (a) overdetermined dual-Doppler (ODD) method and (b) direct method at 6 km height. Reflectivity is plotted in dBZ. Aircraft track relative to data is indicated in Fig. 7. Distances are in km.

Unauthenticated | Downloaded 09/23/21 10:07 AM UTC

be advected to a new apparent position. Note the ODD analysis (Fig. 9a) contains more vectors than the direct solution (Fig. 9b). This is because the direct solution requires that there be data from all three legs. The ODD analysis requires that there be data only from two legs as long as they are not parallel or near parallel. From Fig. 8a we would suspect winds for positions $y \leq 11$ and some of the largest apparent errors appear there. The remarkable feature is the similarity between the windfield synthesized from the ODD and the direct method. The direct method solution at a grid point does not incorporate data from adjacent grid points, so the similarity of winds between grid points reflects the smoothly varying fields within this storm and the accuracy of the analysis. Due to the effects of finite differencing in the computation of divergence and the iterative nature of the solution, there is some correlation between values at adjacent grid points in the ODD method. For both methods the flow is predominately (below about 5 km) from the east on the easternside of the storm. The sea breeze convergence line and updraft location can be seen around $x = 20$. The reflectivity maxima are displaced to the east of this location suggesting that the updraft may tilt downshear (toward the east).

The divergent wind field at 14.4 km height, from the overdetermined method near the storm top, is shown in Fig. 10. The divergence maximum is associated with the reflectivity maxima at this altitude. Stronger upper level westerlies are apparent in the larger vectors ($\sim$20 m s^{-1}) on the eastern portion of the storm. The analysis assumes that this divergence value is representative of the value extending an additional 1.2 km and that the vertical velocity vanishes at a height of 16.8 km, 2.4 km above the depicted level.

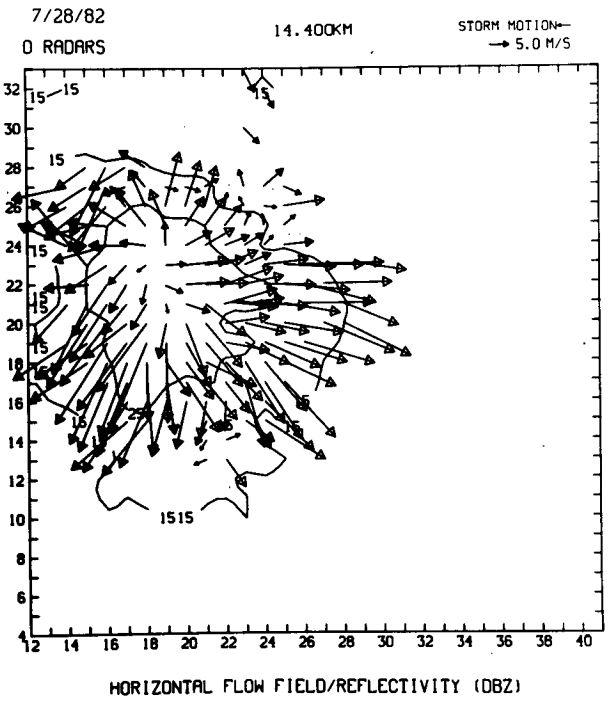

FIG. 10. Horizontal wind at 14.6 km using the overdetermined dual-Doppler method. Reflectivity is in dBZ. Distances are in km and the location of the analysis domain is indicated in Fig. 7.

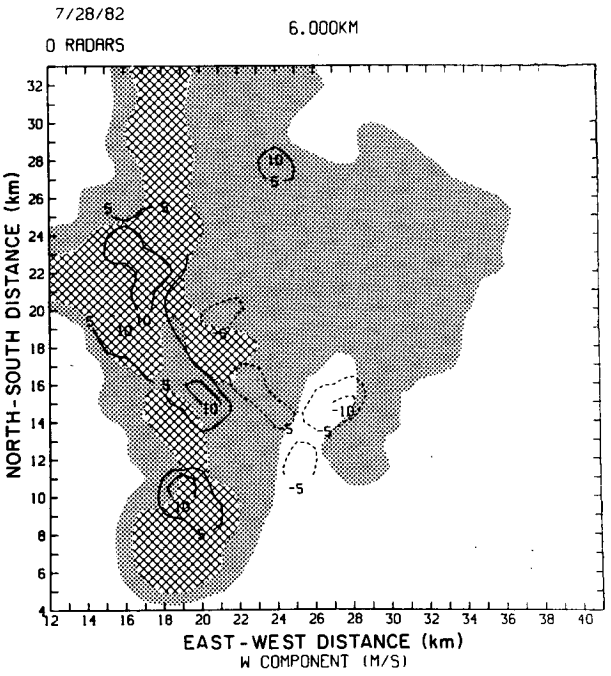

FIG. 11. Contoured vertical motion field at 6 km altitude from overdetermined dual Doppler (ODD) method. Stippling indicates region where reflectivities are between 25 and 35 dBZ. Hatched area indicates reflectivities greater than 35 dBZ.

The vertical motion field at 6 km height from the ODD method is shown in Fig. 11 with the 25–35 dBZ level indicated by stippling. Note that updrafts (typically 10–15 m s^{-1}) exist near the $x = 20$ line noted in Fig. 9 and that at 6 km the reflectivity maxima (35–45 dBZ) are nearly coincident with the updraft maxima. The low level wind field (not shown) shows strong divergence at the surface particularly in the vicinity of what appears to be the main cell at coordinates (20, 20). By about 2 km height the predominant wind is from the south except for $x < 20$ where the winds have a large westerly component. This characterizes the flow up to about 6 km height which is illustrated in Fig. 9. Above this level the winds are strong with a large component out of the northwest. About 12 km diverenge again is the dominant feature in the horizontal flow field.

The vertical structure is shown by an east–west vertical cross section from the ODD method in Fig.

Unauthenticated | Downloaded 09/23/21 10:07 AM UTC

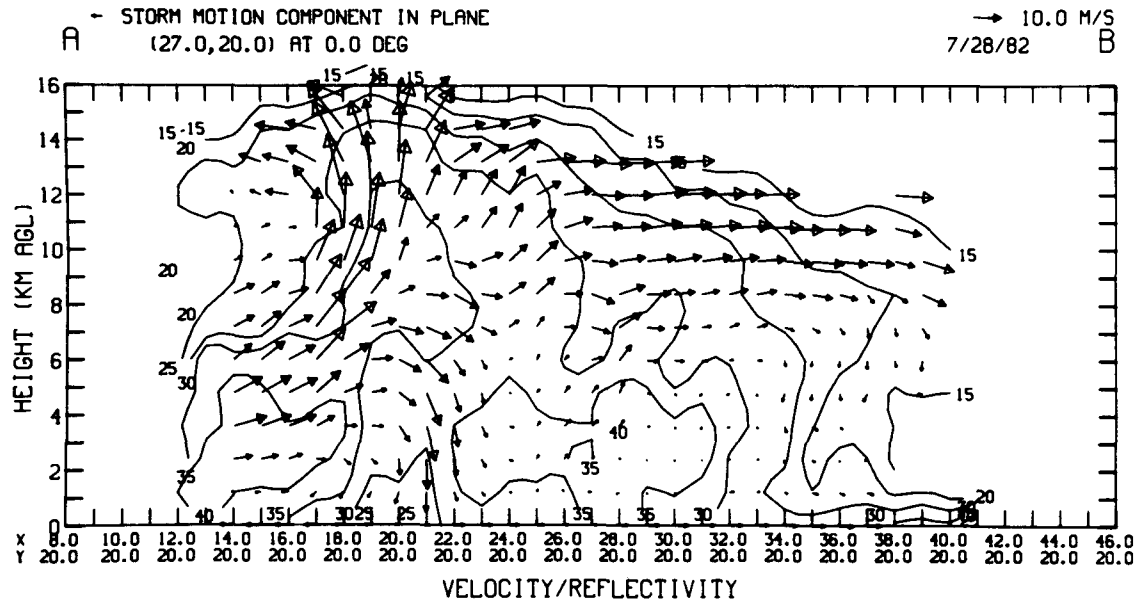

FIG. 12. Vertical cross section of storm relative winds at $y = 20$ from the ODD method. Contours are reflectivity in dBZ in 5 dBZ increments. An arrow one grid length long represents a velocity of 10 m s^{-1}.

12. The east–west oriented cross section shows the wind component in the plane at $y = 20$ km. This traverses the largest updraft in the domain where maximum vertical wind speeds exceed 20 m s^{-1}. In this cross section we can see the low-level divergence near $x = 21$ km, the inflow from the west through a 6 km layer, and the strong divergence at storm top. The reflectivity maxima is displaced slightly down shear from the largest updraft. It appears that many of the hydrometeors produced in the western portion of the storm are advected to the east and that at the eastern edge of the storm weak downdrafts exist over a large depth. The largest downdraft ($x \sim 21$) is nearly below the largest updraft and may reflect the effects of precipitation drag and evaporative cooling.

4. Summary and conclusions

Airborne Doppler radar can economically interrogate a wide variety of storms in regions largely inaccessible to ground-based Doppler networks. Other instrumentation aboard the aircraft complement the radar data. The largest errors in analysis with airborne Doppler radar not seen in ground-based measurements are attributable to uncertainties in aircraft position, orientation (pitch, roll, drift, etc.), and antenna alignment. To a degree, these errors can be corrected. Another source of error for which there is no correction, is the effect of storm evolution during the relatively long time required for data gathering, typically tens of minutes. A second Doppler-equipped aircraft would reduce the time required.

Errors are found to be large close to the flight track when using dual-Doppler analysis methods. These can be explained as a combination of the equivalent ground base radar problem of observing close to the base line or viewing a storm which requires high elevation angles to reach the top. These error fields emphasize the necessity for flying a pattern that maintains a range to the target of interest that is at least as large as the height of the target above (or below) the aircraft flight level so that maximum elevation angles do not exceed ±45°. When at least three observations of a given point are possible from distinctly different angles (≳20°) (usually obtained by flying a box or triangular pattern) then the wind components may be deduced directly. For certain geometries it may be desirable to obtain the vertical motion from integrating the directly synthesized horizontal motion field.

The direct and the overdetermined dual-Doppler method were applied to an airborne Doppler radar observation of a sea-breeze induced convective storm in Florida. Wind fields produced using both methods show strong agreement with each other and consistency among most adjacent grid points. This encouraging result suggests that these wind fields are useful in deducing storm structure. However, in determining which of the possible error analysis is most applicable one must consider more than just the largely geometric propagation of statistical sampling errors. For example, the direct solution method might be expected to be more sensitive to evolution effects since it does not possess the averaging properties of the least-squares

Unauthenticated | Downloaded 09/23/21 10:07 AM UTC

approach. Clearly more work is required to formulate the best combination of sampling (flight) and analysis techniques to fully capitalize on the portability of airborne Doppler radar.

Acknowledgments. The development of NOAA's airborne Doppler radar resulted from the combined work of many engineers and scientists. Bob Trotter of the Weather Modification Program Office of ERL/NOAA did most of the technical modification of the existing receiver, with engineering support by Richard Strauch of NOAA/WPL, Chuck Frush of NCAR, and Dale Sirmans of NOAA/NSSL. Dale Sirmans of NSSL built the pulse pair processor.

Partial support for this work was provided by NSF Grant ATM-8403452.

Appreciation is expressed to Kimberly Banner, Mary Stephenson (of NSSL), and Nancy Figueroa (of HRD) for their assistance in the data analysis. Thanks to Sandra McPherson and Michelle Foster for typing the manuscript and to Joan Kimpel for drafting the figures.

REFERENCES

Haltiner, G. J., and R. T. Williams, 1980: *Numerical Prediction and Dynamical Meteorology.* Wiley & Sons, 477 pp.

Hildebrand, P. H., C. C. Walther, C. Frush and C. Mueller, 1983: Airborne Doppler weather radar: Evaluation and discussion of applications. *Preprints 21st Conf. Radar Meteorology,* Edmonton, Amer. Meteor. Soc., 270–277.

Jorgensen, D. P., 1984: Mesoscale and convective-scale characteristics of mature hurricanes. Part I: General observations by research aircraft. *J. Atmos. Sci.,* **41,** 1268–1285.

——, P. H. Hildebrand and C. L. Frush, 1983: Feasibility test of an airborne pulse-Doppler meteorological radar. *J. Climate Appl. Meteor.,* **22,** 744–757.

Ray, P. S., and K. L. Sangren, 1983: On multiple-Doppler radar network design. *J. Climate Appl. Meteor.,* **22,** 1444–1453.

——, C. L. Ziegler, W. Bumgarner and R. J. Serafin, 1980: Single- and multiple-Doppler radar observations of tornadic storms. *Mon. Wea. Rev.,* **108,** 1607–1625.

Unauthenticated | Downloaded 09/23/21 10:07 AM UTC